PROCEEDINGS of the
23rd International Congress on Acoustics
9 to 13 September 2019 in Aachen, Germany

[Broadband time-domain impedance boundary modeling with the discontinuous Galerkin method for room acoustics simulations]

Huiqing WANG[(1)], Maarten HORNIKX[(1)]

[(1)]Department of the Built Environment, Eindhoven University of Technology, The Netherlands
h.wang6@tue.nl, m.c.j.hornikx@tue.nl

Abstract
The time-domain nodal discontinuous Galerkin method is emerging as a potential wave-based method for three-dimensional (3D) room acoustics modeling, where high-order accuracy, geometrical flexibility and accurate modeling of boundary conditions are of critical importance. In this work, an accurate and efficient formulation of broadband time-domain impedance boundary conditions of locally-reacting surfaces is proposed in the framework of the TD-DG method. The formulation of the time-domain boundary condition is based on the plane-wave reflection coefficient at normal incidence and its approximation in the frequency domain using a sum of rational fractions, which can be obtained from analytical models or measured impedance values. To verify the performance of the formulation, a single reflection scenario is considered. The reflection coefficient obtained from the numerical tests is compared with the analytical one based on a locally reacting surface impedance with a typical impedance model of a rigid frame porous material for room acoustic uses. It is demonstrated that both the amplitude and the phase of the reflection behavior are accurately predicted.
Keywords: Room acoustics modeling, time-domain impedance boundary condition, Discontinuous Galerkin method

1 INTRODUCTION

In general, room acoustic modeling techniques can be divided into two categories, namely geometrical acoustics methods and the wave-based methods. Wave-based methods in the time-domain are becoming more and more widely used for design purposes (17). Recently, the time-domain discontinuous Galerkin (DG) method has for the first time been evaluated as a potential wave-based method for room acoustics modeling purposes (19). Its high-order accuracy and the ability to handle complex boundary geometries are demonstrated through verifications by analytical solutions and validation against measurement results of a real room.
This paper focuses on the numerical implementation of a generic broadband time-domain impedance boundary condition within the DG framework. A novel numerical flux formulation along the impedance boundary surface is derived based on the plane wave reflection coefficient and the characteristic acoustic waves. Compared to the conventional approach that uses the impedance value, this formulation allows a fully-discrete CFL stability condition that is independent of the frequency-independent impedance value. The extension of previous frequency-independent impedance boundary formulation to the frequency-dependent one is achieved through the multi-pole representation of the reflection coefficient in the frequency domain, which consists of a sum of first order systems (real poles) or second order systems (complex conjugated poles) (7, 13). The parameter fitting for a general impedance model or data is achieved by solving an optimization problem. Combined with the auxiliary differential equations (ADE) method, the whole formulation can be performed in a low-storage and high-order accuracy manner. To validate this formulation, numerical simulations of a single reflection scenario are performed. Both the amplitude and the phase error from the reflection, which are important for room acoustics modeling featuring multiple reflections, are investigated and quantified for the spherical wave reflection in a 3-D case with respect to different points per wavelength. Application to a typical impedance model of a rigid frame porous material for room acoustic uses is used to demonstrate the feasibility of the proposed approach.

The paper is organized as follows. The novel formulations of impedance boundary conditions within the time-domain DG method are presented in Sec. 2. Sec. 3 quantifies and discusses the accuracy of the implemented formulation by comparison with the analytical solutions. Finally, conclusions and outlook can be found in Sec. 4.

2 TIME-DOMAIN IMPEDANCE BOUNDARY CONDITIONS IN DG

2.1 Governing equations and time-domain DG method

In this work, the governing equations are the linear acoustic equations for a motionless propagation medium

$$\begin{aligned} \frac{\partial v}{\partial t} + \frac{1}{\rho}\nabla p = 0, \\ \frac{\partial p}{\partial t} + \rho c^2 \nabla \cdot v = 0, \end{aligned} \tag{1}$$

where $v = [u,v,w]^T$ is the particle velocity vector, p is the sound pressure, ρ is the constant density of air and c is the constant speed of sound. Equivalently, Eqs. (1) read

$$\frac{\partial q}{\partial t} + \nabla \cdot F(q) = \frac{\partial q}{\partial t} + A_j \frac{\partial q}{\partial x_j} = 0, \tag{2}$$

where $q(x,t) = [u,v,w,p]^{\mathrm{T}}$ is the acoustic variable vector and A_j is the constant flux Jacobian matrix with coordinate index $j \in [x,y,z]$. The physical domain is divided into K non-overlapping elements of a certain type, e.g. tethrahedra. The local numerical solution $q_h^k(x,t)$ in element D^k is given by

$$q_h^k(x,t) = \sum_{i=1}^{N_p} q_h^k(x_i^k,t) l_i^k(x), \tag{3}$$

where $q_h^k(x_i^k,t)$ are the unknown nodal values and $l_i^k(x_i^k)$ is the multi-dimensional Lagrange polynomial basis of order N, which satisfies $l_i^k(x_j^k) = \delta_{ij}$. N_p is the number of local basis functions (or nodes) inside a single element and equal to $(N+d)!/(N!d!)$ for simplex elements, where d is the dimensionality. The semi-discrete nodal DG formulation of Eq. (2) reads:

$$\int_{D^k} \left(\frac{\partial q_h^k}{\partial t} + \nabla \cdot F_h^k(q_h^k) \right) l_i^k \mathrm{d}x = \int_{\partial D^k} n \cdot \left(F_h^k(q_h^k) - F^* \right) l_i^k \mathrm{d}x, \tag{4}$$

where $n = [n_x, n_y, n_z]$ is the outward normal vector of the element surface ∂D^k. F^*, the so-called numerical flux across element intersection ∂D^k, is a function of both the solution value from the interior side of the intersection, i.e., q_h^- and the exterior value q_h^+. In this study, the upwind numerical flux is used throughout the whole domain because of its low dispersive and dissipation error (1, 11). It is defined by considering the direction of the characteristic speed, i.e.,

$$n \cdot F^*(q_h^-, q_h^+) = L(\Lambda^+ L^{-1} q_h^- + \Lambda^- L^{-1} q_h^+), \tag{5}$$

where Λ is a diagonal matrix with diganoal entries $[0,0,c,-c]$. Λ^+ and Λ^- contain the positive and negative entries of Λ respectively. L is the eigenmatrix of the normally projected flux Jacobian, i.e.,

$$\begin{aligned} A_n &= (n_x A_x + n_y A_y + n_z A_z) \\ &= L \Lambda L^{-1}. \end{aligned} \tag{6}$$

Physically, Λ^+ (Λ^- respectively) corresponds to the characteristic waves propagating along (opposite to respectively) the outward normal direction n, which are referred to as outgoing waves out of D_k (incoming

waves into D_k respectively). Therefore, the outgoing waves are associated with the interior solution q_h^- whereas the incoming waves are dependent on the exterior (neighboring) solution q_h^+. After the spatial discretization by the nodal DG method, the semi-discrete system can be time-integrated using low-storage explicit Runge-Kutta (RK) schemes (3, 18). More detailed descriptions of the time-domain nodal discontinuous Galerkin method for the linear acoustic equations are available in Ref. (19) and in-depth discussions of the DG method can be found in Ref. (9).

2.2 Numerical flux formulation of TDIBC

The essential idea of the impedance boundary condition formulation is to reformulate the numerical flux normal to the impedance boundary surface based on the characteristic waves of the linear acoustic equations and the reflection coefficient R. The incoming and outgoing characteristic acoustic waves, which are denoted as ϖ_n^{in} and ϖ_n^{out}, and oriented in the opposite and the same direction of the outward normal n along the boundary surface respectively, are defined as

$$\varpi_n^{in}(\omega) = \frac{p(\omega)}{\rho c} - v_n(\omega) \tag{7}$$

$$\varpi_n^{out}(\omega) = \frac{p(\omega)}{\rho c} + v_n(\omega). \tag{8}$$

The plane wave reflection coefficient $R(\omega)$ at normal incidence angle satisfies (14)

$$R(\omega) = \frac{Z_s(\omega) - 1}{Z_s(\omega) + 1}. \tag{9}$$

By the definition of the normalized surface impedance Z_s, *i.e.,* $Z_s(\omega) = p(\omega)/(v_n(\omega)\rho c)$ and Eq. (9), the following condition concerning the reflection coefficient and characteristic waves is yielded

$$R(\omega) = \frac{\varpi_n^{in}(\omega)}{\varpi_n^{out}(\omega)}. \tag{10}$$

The time-domain implementation of the impedance boundary condition is realized by coupling the above condition Eq. (10) with the DG discretization through the reformulation of the upwind flux near the boundaries. The use of the plane wave reflection coefficient at normal incidence is consistent with the fact that the numerical flux from the nodal DG scheme is always normal to the boundary surface. The frequency-dependency of the impedance model is introduced through the use of the multi-pole approximation of the plane wave reflection coefficient. The whole TDIBC formulation consists of three steps. The first step is to transform the impedance values $Z_s(\omega)$, which can be obtained from either a continuous impedance model or from measured discrete impedance values within the interested frequency range, to the corresponding normal reflection coefficient $R(\omega)$ using Eq. (9). Secondly, the target reflection coefficient $R(\omega)$ is approximated with a sum of rational functions (6)

$$R(\omega) \approx R_\infty + \sum_{k=1}^{S} \frac{A_k}{\zeta_k + \mathrm{i}\omega} + \sum_{l=1}^{T} \frac{1}{2}\left(\frac{B_l - \mathrm{i}C_l}{\alpha_l - \mathrm{i}\beta_l + \mathrm{i}\omega} + \frac{B_l + \mathrm{i}C_l}{\alpha_l + \mathrm{i}\beta_l + \mathrm{i}\omega} \right)$$

where $[R_\infty, A_k, B_l, C_l, \zeta_k, \alpha_l, \beta_l] \in \mathbb{R}$ are all real numerical parameters that fit the plane wave reflection coefficient for normal incident sound waves. To be more specific, R_∞ is the limit value of $R(\omega)$ as the frequency approaches infinity. ζ_k and $\alpha_l \pm \mathrm{i}\beta_l$ are the real poles and complex conjugate pole pairs respectively. To satisfy the causality and reality condition, $\zeta_k, \alpha_l, \beta_l$ need to be positive, and the passivity condition is fulfilled when $|R_n(\omega)| \leq 1$ (5). In this work, the convention of $\mathrm{e}^{\mathrm{i}\omega t}$ is used for the harmonic time variation.
In the time-domain, the so-called reflection impulse response function is written as

$$R(t) \approx R_\infty \delta(t) + \sum_{k=1}^{S} A_k \mathrm{e}^{-\zeta_k t} H(t) + \sum_{l=1}^{T} \mathrm{e}^{-\alpha_l t} \left(B_l \cos(\beta_l t) + C_l \sin(\beta_l t) \right) H(t), \tag{11}$$

where $\delta(t)$ and $H(t)$ are the Dirac delta and Heaviside function respectively. As shown in Ref. (6), each term in $R(t)$ has a physical interpretation. The first term of Eq. (11) stands for the instantaneous response, since R_∞ is the frequency independent value or high-frequency limit of $R(\omega)$. The second term is a exponentially decaying relaxation function, which mimics the absorption behavior of porous materials. The last group of terms are the so-called damped multi-oscillators that can be linked to resonator-type absorbers, where the imaginary part of the pole β_l determines the oscillation period and the real part α_l governs the decaying rate.

The third and last step of the proposed TDIBC formulation in DG is to enforce the multi-pole impedance model into the numerical flux along the impedance boundary surface. For this purpose, the time-domain counterpart of the characteristic acoustic waves as defined in Eqs. (7,8) has to be obtained, by pre-multiplying the acoustic variables q with the left eigenmatrix L^{-1}, i.e.,

$$L^{-1}q = \begin{bmatrix} 0 \\ 0 \\ \varpi_n^{out}(t) \\ \varpi_n^{in}(t) \end{bmatrix} = \begin{bmatrix} 0 \\ 0 \\ \frac{p(t)}{\rho c} + v_n(t) \\ \frac{p(t)}{\rho c} - v_n(t) \end{bmatrix}. \tag{12}$$

It should be noted that the first two characteristic terms in the above equation (12) are numerically irrelevant in the whole boundary formulation, since their characteristic speeds (the first two diagonal values in Λ) are zero. Finally, the numerical flux formulation of the TDIBC is given as

$$n \cdot F^*(q_h^-) = L\Lambda[0, 0, \varpi_n^{out}(t), \varpi_n^{in}(t)]^{\mathrm{T}} \tag{13}$$

where $\varpi_n^{out}(t)$ can be firstly calculated with the interior solution values at each of discrete nodes along the boundary as

$$\varpi_n^{out}(t) = \frac{p^-(t)}{\rho c} + v_n^-(t), \tag{14}$$

and then based on the condition of Eq. (10), $\varpi_n^{in}(t)$ is obtained from the convolution of $\varpi_n^{out}(t)$ with $R(t)$ of Eq. (11)

$$\varpi_n^{in}(t) = \int_{-\infty}^{t} \varpi_n^{out}(\tau) R(t-\tau) \mathrm{d}\tau. \tag{15}$$

To compute the convolution Eq. (15) in a time efficient and low-storage manner, the auxiliary differential equations (ADE) method, originally developed by Joseph et al. (12) for electromagnetic applications, is employed in this study. Firstly, substitution of the reflection impulse response $R(t)$ given in Eq. (11) into Eq. (15) yields

$$\varpi_n^{in}(t) = R_\infty \varpi_n^{out}(t) + \sum_{k=1}^{S} A_k \phi_k(t) + \sum_{l=1}^{T} [B_l \psi_l^1(t) + C_l \psi_l^2(t)], \tag{16}$$

where the new terms $\phi_k(t), \psi_l^1(t), \psi_l^2(t)$, referred to as accumulators or auxiliary variables are calculated by solving the the following first-order ordinary differential equations

$$\frac{\partial \phi_k}{\partial t} + \zeta_k \phi_k(t) = \varpi_n^{out}(t), \tag{17}$$

$$\frac{\partial \psi_l^1}{\partial t} + \alpha_l \psi_l^1(t) + \beta_l \psi_l^2(t) = \varpi_n^{out}(t), \tag{18}$$

$$\frac{\partial \psi_l^2}{\partial t} + \alpha_l \psi_l^2(t) - \beta_l \psi_l^1(t) = 0. \tag{19}$$

The above system is numerically integrated from zero initial values using the same time-integration scheme as for the semi-discrete DG formulation Eq. (4). As shown by Dragna et al. (6), the ADE method has the

benefit of keeping the same order accuracy of a general multi-stage time integration scheme. Furthermore, low memory space is needed since these accumulators only exist on the boundary nodes. In this work, a low-storage explicit 5-stages Runge-Kutta developed by Carpenter and Kennedy (3), denoted as RK5 hereafter, is used.

3 3D NUMERICAL TESTS

To verify the proposed formulation of the TDIBC and quantify both the dissipation and dispersion error, a single reflection scenario is considered and the reflection coefficient obtained from the numerical tests is compared with the analytical one. The experiment consists of two simulations, which are initiated with the same Gaussian-shaped pressure conditions:

$$p(x,t=0) = \mathrm{e}^{\frac{-\ln 2}{b^2}(x-x_s)^2}, \tag{20a}$$

$$v(x,t=0) = 0, \tag{20b}$$

with x_s the source coordinates and $b = 0.25$ the half-bandwidth of this Gaussian pulse. To get the direct sound, a cubic domain of size $[-8,8]^3$ in meter is considered, where the Gaussian pressure pulse is centered at $x_s = [0,0,0]$ m, and two receivers are placed at $x_{r1} = [0,0,-1]$ m and $x_{r2} = [0,4,-1]$ m. In the second simulation, a plane reflecting surface is placed 2 m away from the source at $z = -2$ m. The simulation is run for a non-dimensional time of $\bar{t} = t \cdot c = 11$, $\bar{t} = t/(l_{ref}/c) = 11$, to avoid the waves above a certain frequency threshold value being reflected from the exterior boundaries of the whole domain. Structured tetrahedra meshes are used for this study to avoid the mesh quality issue, which are generated with the meshing software GMSH (8) . The whole cuboid domain is contained of structured cubes of the same size, then each cube is split into 6 tetrahedra elements. The length of each cube is 0.5 m. The number of degrees of freedom per wavelength l_λ (DPW) is used to give a practical indication of the computational overhead of the DG method, which is computed as $DPW = l_\lambda \left(N_p \cdot K/V\right)^{1/d}$, where $N_p \cdot K$ is the number of degrees of freedom for a single physical variable in the computational domain and V is the volume of the whole domain. The time steps are determined in the following way:

$$\Delta t = C_{CFL} \cdot \min(\Delta x_l) \cdot \frac{1}{c} \cdot \frac{1}{N^2}, \tag{21}$$

where Δx_l is the edge length of the tetrahedra elements of mesh. Simulations with a polynomial basis of order $N = 7$ and $C_{CFL} = 0.5$ are performed, with the corresponding DPW=10.2 for the frequency of 600 Hz. In the first simulation, the direct sound signal, denoted as $p_d(t)$, is recorded. In the second simulation, a reflecting surface is present and the measured sound pressure signals contains both the direct sound and the sound reflected from the impedance surface. The reflected sound signal $p_r(t)$ can be obtained by subtracting $p_d(t)$. The spectra of the direct sound and the reflected sound, denoted as $P_d(f)$ and $P_r(f)$ respectively, are obtained by Fourier transforming p_d and p_r without windowing. Let R_1 denote the distance between the source and the receiver and R_2 is the distance between the receiver and the image source mirrored by the reflecting impedance surface. The numerical spherical wave reflection coefficient R_{num} is then calculated as follows:

$$R_{num}(f) = \frac{P_r(f) \cdot G(kR_1)}{P_d(f) \cdot G(kR_2)}, \tag{22}$$

where $G(kR)$ is the 3-D Green's function for free field propagation and k is the wavenumber. The dissipation error ε_{amp} in dB and the phase error ε_ϑ in % from a single reflection are calculated as follows

$$\varepsilon_{amp}(f) = 20\log_{10}\left|\frac{R_{ana}(f)}{R_{num}(f)}\right|, \tag{23a}$$

$$\varepsilon_\vartheta(f) = \frac{1}{\pi}\left|\vartheta\left(R_{ana}(f)\right) - \vartheta\left(R_{num}(f)\right)\right| \times 100\%, \tag{23b}$$

where $\vartheta(\cdot)$ extracts the phase angle of a complex number and R_{ana} is the analytical spherical wave reflection coefficient that can be found in Ref. (4). Therefore, for a given broadband incident acoustic wave of arbitrary amplitude, the loss of SPL and the distortion of the phase across the frequency range of interest can be quantified.

For the surface material, we consider acoustic baffles that can be modelled by the Johnson-Champoux-Allard-Lafarge (JCAL) model (15) , which is a phenomenological model considering wave propagations in porous materials on a microscopic scale. The characteristic impedance Z_c reads $Z_c = \sqrt{\rho_{eff}\varkappa_{eff}}$ where ρ_{eff} is the effective density and $\varkappa_{eff}$ is the effective bulk modulus. The baffles with thickness d can be backed by a rigid layer, then the surface impedance becomes

$$Z = -\mathrm{i}Z_c \cot(k_{eff}d), \tag{24}$$

where the wavenumber of the porous material is given as $k_{eff} = \omega\sqrt{\rho_{eff}/\varkappa_{eff}}$. In this study, one particular set of physical parameters and their values for a typical glass wool material measured from experiments (10) is used.

In order to fit the multi-pole representation of the reflection coefficient $R(\omega)$, which is obtained from a transformation of impedance Z_s by Eq. (9), the optimization technique with the interior-point algorithm (2) from the MATLAB optimization toolbox (16) is used. For the JCAL model considered, it is sufficient to use real poles alone since the absorption coefficient increases monotonously with the frequency. The fitted reflection coefficient is plotted in Fig. 1.

Now, the numerical reflection coefficients are verified directly against the analytical one governed by the

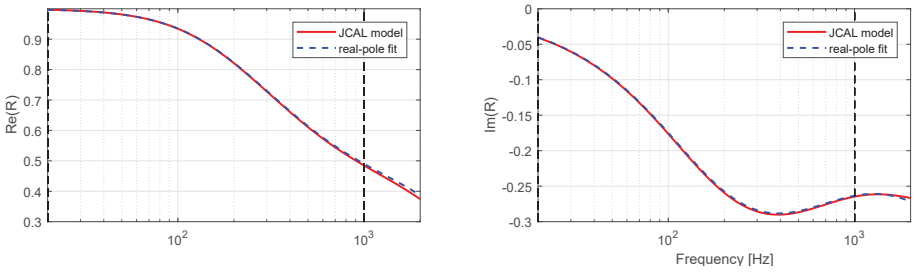

Figure 1. Multi-pole fitting of real and imaginary part of the normal incidence reflection coefficient of a rigidly-backed layer represented by the JCAL model in the frequency range 20-1000 Hz.

JCAL model as prescribed in Eq. (24). The dissipation error ε_{amp} in dB, the phase error ε_{ϑ} in % and the amplitude of both the analytical and numerical spherical wave reflection coefficient are shown in Fig. 2 for both the normal incidence ($\theta = 0°$) and the oblique incidence ($\theta = 53°$) cases. It can be seen that the numerical reflection coefficient matches the analytical one in terms of both the magnitude and the phase angle. It should be mentioned that the error under the oblique incidence case is larger than the one under the normal incidence. Numerical tests have found that these discrepancies can be partly attributed to the longer travelling distance between the source and the receiver for the oblique incidence case, which introduces more error from the propagation for both the direct and the reflected sound. Another source of error comes from the multi-pole fitting of the plane wave reflection coefficient of the JCAL model, which does not strictly decrease with increasing DPW.

4 CONCLUSIONS

In this work, a novel numerical formulation for the time-domain impedance boundary condition implementations in the framework of the time-domain DG method is developed for the simulation of broadband sound

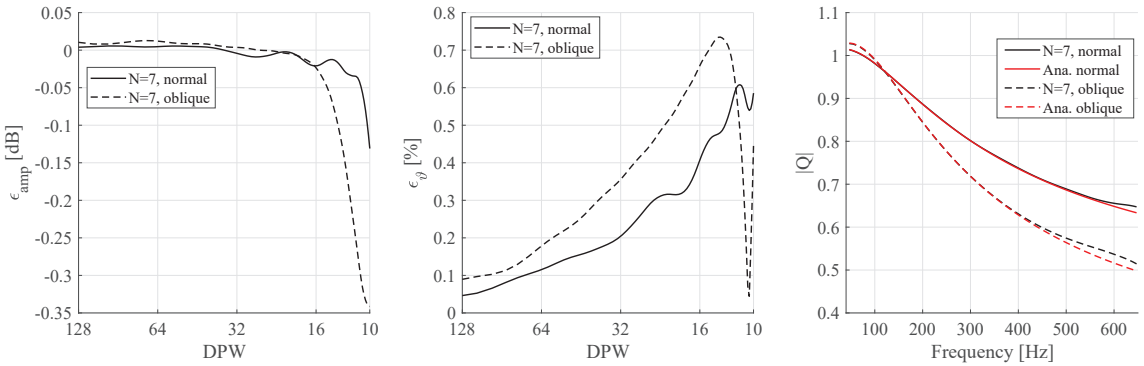

Figure 2. The dissipation error ε_{amp}, the phase error ε_ϑ and the amplitude of the spherical wave reflection coefficient from the multi-pole fit verified against the exact JCAL model.

propagation problems, specially targeting at the room acoustic applications. The essential idea is to model the acoustic reflection behavior of a locally-reacting surface using the reflection coefficient $R(\omega)$ in the form of a multi-pole model and then reformulate the corresponding time domain upwind flux. This work is an extension of previous frequency-independent impedance boundary formulation to a generic broadband one. A straightforward and effective parameter identification strategy is presented together with an example application to a typical impedance model of a glass-wool baffle for room acoustic purposes.
To verify the performance of the formulation, the reflection coefficients obtained from numerical tests are compared with the analytical ones. The three-dimensional tests demonstrate the capacity of the proposed methodology. To sum up, the proposed method is quite straightforward in formulation, easy to implement and therefore further strengthens the potential of the time-domain discontinuous Galerkin method as a wave-based method for room acoustics modeling.

ACKNOWLEDGMENTS

This project has received funding from the European Union's Horizon 2020 research and innovation programme under grant agreement No. 721536.

REFERENCES

[1] M. Ainsworth. Dispersive and dissipative behaviour of high order discontinuous Galerkin finite element methods. *Journal of Computational Physics*, 198(1):106–130, 2004.

[2] R. H. Byrd, M. E. Hribar, and J. Nocedal. An interior point algorithm for large-scale nonlinear programming. *SIAM Journal on Optimization*, 9(4):877–900, 1999.

[3] M. H. Carpenter and C. A. Kennedy. Fourth-order 2N-storage Runge-Kutta schemes. In *NASA-TM-109112*, 1994.

[4] X. Di and K. E. Gilbert. An exact Laplace transform formulation for a point source above a ground surface. *The Journal of the Acoustical Society of America*, 93(2):714–720, 1993.

[5] Q. Douasbin, C. Scalo, L. Selle, and T. Poinsot. Delayed-time domain impedance boundary conditions (d-tdibc). *Journal of Computational Physics*, 371:50–66, 2018.

[6] D. Dragna, P. Pineau, and P. Blanc-Benon. A generalized recursive convolution method for time-domain propagation in porous media. *The Journal of the Acoustical Society of America*, 138(2):1030–1042, 2015.

[7] K.-Y. Fung and H. Ju. Broadband time-domain impedance models. *AIAA journal*, 39(8):1449–1454, 2001.

[8] C. Geuzaine and J.-F. Remacle. Gmsh: A 3-D finite element mesh generator with built-in pre-and post-processing facilities. *International Journal for Numerical Methods in Engineering*, 79(11):1309–1331, 2009.

[9] J. S. Hesthaven and T. Warburton. *Nodal discontinuous Galerkin methods: Algorithms, Analysis and Applications*. Springer-Verlag, New York, 2007.

[10] N. Hoeskstra. *Sound absorption of periodically spaced baffles*. Master thesis, Eindhoven University of Techonology, 2016.

[11] F. Hu and H. Atkins. Two-dimensional wave analysis of the discontinuous Galerkin method with non-uniform grids and boundary conditions. In *8th AIAA/CEAS Aeroacoustics Conference & Exhibit*, page 2514, 2002.

[12] R. M. Joseph, S. C. Hagness, and A. Taflove. Direct time integration of maxwell's equations in linear dispersive media with absorption for scattering and propagation of femtosecond electromagnetic pulses. *Optics Letters*, 16(18):1412–1414, 1991.

[13] H. Ju and K.-Y. Fung. Time-domain simulation of acoustic sources over an impedance plane. *Journal of computational acoustics*, 10(03):311–329, 2002.

[14] H. Kuttruff. *Room acoustics*. CRC Press, New York, 2016.

[15] D. Lafarge, P. Lemarinier, J. F. Allard, and V. Tarnow. Dynamic compressibility of air in porous structures at audible frequencies. *The Journal of the Acoustical Society of America*, 102(4):1995–2006, 1997.

[16] *MATLAB Optimization Toolbox (R2018b)*. The MathWorks, Inc., Natick, Massachusetts, USA, 2018.

[17] T. Sakuma, S. Sakamoto, and T. Otsuru. *Computational simulation in architectural and environmental acoustics*. Springer, 2014.

[18] T. Toulorge and W. Desmet. Optimal Runge-Kutta schemes for discontinuous Galerkin space discretizations applied to wave propagation problems. *Journal of Computational Physics*, 231(4):2067–2091, 2012.

[19] H. Wang, I. Sihar, R. Pagán Muñoz, and M. Hornikx. Room acoustics modelling in the time-domain with the nodal discontinuous galerkin method. *The Journal of the Acoustical Society of America*, 145(4):2650–2663, 2019.